CRYSTAL GROWTH & DESIGN

pubs.acs.org/crystal

Article

Formation of Macrotubular Crystals of Salicylic Acid through Ripening of Solid Solution Crystals Containing Impurity Gradients

Yongjian Wang, Huayu Li, Michelle Raikes, Brian Linehan, John Robson, and Fredrik L. Nordstrom*

Cite This: *Cryst. Growth Des.* 2021, 21, 4100–4110

Read Online

ACCESS | Metrics & More | Article Recommendations | Supporting Information

ABSTRACT: We report a ripening mechanism in crystallization of an organic compound that is observable above 1 μm and is different from Ostwald ripening. Salicylic acid crystallized in methanol and water in the presence of simulated structurally similar impurities resulted in impurity entrapment *via* the formation of solid solutions. Impurities were retained in the solids to a higher degree in the early part of the crystallization and decreased rapidly toward the end. This uneven impurity entrapment resulted in impurity gradients in individual crystals, which were detected and confirmed by Raman imaging. The impurity entrapment impacted the physical properties of salicylic acid, including its solubility and melting properties. An intra-particle thermodynamic driving force was thus found to exist during the crystallization, which caused selective dissolution of the dirtier cores of the crystal and recrystallization on the cleaner edges. These concomitant but opposing mass transfer processes during the crystallization were responsible for the formation of hollow crystals of salicylic acid. The ripening phenomenon is demonstrated experimentally in the beginning and end of an isothermal anti-solvent crystallization as well as during an agitated filter dryer operation.

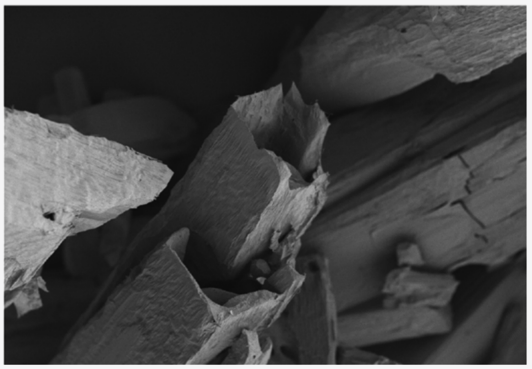

INTRODUCTION

The first ripening mechanism in crystallization was reported by Wilhem Ostwald over a century ago[1,2] and described the process by which larger crystals grow on the expense of smaller crystals. The now famous Ostwald–Freundlich equation[3,4] was later derived showing the direct relationship of the solubility of a particle relative to its size. This relationship has been widely used to understand physical processes at the nanoscale, including crystallization from the solution. As an example, the classical nucleation theory was originally developed by Gibbs[5] and Volmer and Weber[6] using the same relations. However, once crystals exceed a certain size, the influence of Ostwald ripening diminishes. For the organic compound glycine, it was reported that its solubility remains mostly unchanged above around 1 μm size.[7] Dissolution and recrystallization processes of organic crystals above this size range can therefore not be attributed directly to Ostwald ripening. Nevertheless, changes in physical properties of pharmaceutical compounds are sometimes observed during so-called hold points in crystallization processing, even when micron-sized crystals suspended in a solvent are seemingly under equilibrium conditions. This extends to macrotubular crystals, which contain empty cavities up to several μm within individual particles. While these hollow crystals are known to appear for metals,[8,9] they have recently attracted a great deal of attention for organic and pharmaceutical compounds owing to their high surface area, unique morphology, and enhanced dissolution rate. The pharmaceutical compound dexamethasone acetate was found to form macrotubular crystals in 2004.[10] Salicylic acid (SA), the compound of focus in this study, was similarly reported in 2006[11] to crystallize with hollow voids in the center, which was also investigated by Seidel and Ulrich, 2015[12] and Tierney *et al.*, 2017.[13] Many other examples are now known covering a wide spectrum of organic compounds,[14−19] which speaks to the generality of this intriguing morphology and the many potential applications in the pharmaceutical industry and elsewhere.

The mechanism behind the formation of tubular crystals has generally been explained by a selective dissolution (or etching) and recrystallization process.[13,16] The reason for this self-assembly by two simultaneous but opposing mass-transfer mechanisms has not been clearly established but hypothesized to be due to surface or crystal defects linked to anisotropic crystal growth. Other explanations relate to the formation of metastable phases as precursors to forming tubular structures[9,20] or the formation of lamellar structures.[18] Influencing parameters for generating tubular structures have been reported to be solvent composition, concentration, super-

Received: April 6, 2021
Revised: May 19, 2021
Published: June 1, 2021

saturation ratio, and mixing. Also, larger crystals are known to carry more indentations and cavities.[13] It should be noted that in each of the reported cases, little attention has been paid to the impact of impurities. Typically, materials were used as is from the vendor without further purification. Impurities are known to have a profound influence on crystallization even at ppm concentrations,[21] and in a recent contribution,[22] it was shown how certain structurally similar impurities become incorporated into SA by forming solid solutions. The early part of the crystallization, that is, directly after seeding, exhibited a higher level of impurity entrapment, while the latter part of the crystallization was associated with lower impurity retention. As a result, the final crystals were composed of gradients in purity starting from a dirty core and becoming progressively cleaner in the radial direction until having the highest purity in the outer layers of the crystals. The extent of entrapment correlated with an increase in solubility, which varied by a factor of 2 across the same material. Thus, it was expected that an intra-particle driving force should exist stemming from differences in solubilities due to variable impurity levels, which would enable dissolution of the dirtier regions of the crystals and lead to recrystallization on the purer areas. This mechanism would thus be different from the traditional Ostwald ripening and in effect across a wide range of crystal sizes.

The objective of this contribution is to demonstrate experimentally and mechanistically how this ripening by simultaneous dissolution and recrystallization takes place throughout the crystallization and is caused by gradients in purity levels in the crystals, which in the case of SA results in the formation of tubular crystals.

EXPERIMENTAL SECTION

Materials. SA (≥99.0%), benzoic acid (BA, 99%), anthranilic acid (AA, ≥98.0%), 2,3-dihydrobenzoic acid (23DHBA, 99%), 3-hydrobenzoic acid (3HBA, 99%), 4-hydrobenzoic acid (4HBA, ≥99.0%), methanol (MeOH, HPLC grade), and water (HPLC grade) were purchased from Millipore Sigma. Acetonitrile (HPLC grade) was purchased from Fisher Scientific. Deionized (DI) water was obtained from an in-house system.

HPLC Method. Samples were analyzed using an Agilent Eclipse Plus phenyl−hexyl (3.0 × 100 mm, 3.5 μm) column at a 0.7 mL/min flow rate, a 55 °C column temperature, an 8 min run time, a 10 μL injection volume, and 280 nm UV detection. The mobile phase consisted of 0.1% H_3PO_4 (mobile phase A) and acetonitrile (mobile phase B). The mobile phase of 90 A/10 B was injected at the beginning and switched to 20 A/80 B at 6 min for 0.1 min, then returning to 90 A/10 B for the rest of the analysis. The data were obtained and analyzed by Empower. The response factors for SA, 23DBA, 3HBA, 4HBA, AA, and BA were 6.360 × 106, 2.419 × 106, 6.061 × 106, 2.050 × 107, 2.462 × 106, and 4.719 × 106, respectively. Linear regression between peak area and concentration showed R^2 > 0.99 for all the compounds.

Crystallization in Example 1. 3.00 g of SA and 66.7 mg of five different impurities (4HBA, 3HBA, 23DBA, AA, and BA), corresponding to a total of 10 wt % impurities, were dissolved in 27.7 g of methanol at ambient temperature in a Metter Toledo EasyMax 102. 41.6 g of water was added to reach a supersaturation ratio of 1.8 at 40 wt % methanol in water. Approx. 0.01% ground pure SA seeds (<1 mg) were added to induce secondary nucleation, and the slurry was stirred at 300 rpm. The samples were collected at 1.5, 7, 17 min, 1, and 2 h after seeding. The solid samples were dried by centrifugation (Eppendorf Centrifuge 5415D, 2 min, 13,200 rpm), and the liquid samples were collected using a syringe. The liquid samples were filtrated using a 0.2 μm filter before being analyzed by HPLC. The entire crystallization was stirred at 300 rpm and room temperature. The samples were diluted with 90 w/w % water (HPLC grade) in acetonitrile for the HPLC analyses.

Crystallization in Example 2. 3.00 g of SA and 158 mg of BA, corresponding to 5.0 wt %, were dissolved in 11.0 g of methanol in a Metter Toledo EasyMax 102. 7.3 g of DI water was added to the clear solution to reach a supersaturation ratio of 1.4 at 60 wt % methanol in water. 0.01% ground pure SA was added as seeds, and the system was stirred at 250 rpm. 18.3 g of DI water was added at 1.0 mL/min right after seeding using an automated anti-solvent dosing unit SP-50 with a 25 mL syringe to reach 30 wt % methanol in water. Samples were collected using the same method above at 15, 90 min, 24, 48, and 120 h after reaching the final solvent composition. The entire crystallization was stirred at 250 rpm and room temperature. The samples were diluted with 90 w/w % water (HPLC grade) in acetonitrile for the HPLC analyses.

Agitated Filter Drying in Example 3. Solids were prepared using the procedure outlined under example 2 above. However, the solids were filtered after the water addition was completed and subsequently dried under vacuum. The dried solids were then reslurried at 5 L water/kg solid either using an overhead stirrer in a Metter Toledo EasyMax 102 or by inserting an IKA T25 wet mill. Samples were pulled of the solid and liquid phases over time and analyzed by HPLC.

Preparation of Purified SA. SA from Sigma-Aldrich was purified twice by recrystallization in MeOH/H_2O without added impurities. 3.0 g of SA was dissolved in 11.0 g of MeOH. 7.3 g of water was added to produce a supersaturation ratio of 1.4. 0.01% ground seed was added to the solution, and then, 18.3 g of DI water was added at 1 mL/min to reach 30% MeOH in H_2O. Approximately 86% yield was obtained. The purified SA was then used as a starting material in the crystallizations in examples 1 and 2 above.

SLIP Test. The samples were suspended in amber vials using 20 wt % methanol in water with different process volumes at room temperature. The vials were capped and parafilmed, and no stirrers were added. The suspensions were equilibrated for 1 h at room temperature on a rotating rack before being filtered and analyzed by HPLC.

Transmission Raman Spectroscopy. Approximately 50 mg of samples was analyzed using an Agilent Transmission Raman spectrometer (TRS100) equipped with a 830 nm laser. Samples were placed in a poly bag and transferred to a sample tray. Raman reference spectra of pure SA and BA were recorded using the material as is from the vendor. The laser power was set at 650 mW with a laser spot size of 4 mm. Spectral data were obtained over a spectral range of 50 to 2500 cm^{-1} with an exposure time of 0.3 s and 20 accumulations using Content QC software.

Confocal Raman Imaging. Analysis of individual crystals was performed on a WITec alpha300 R confocal Raman imaging spectrometer equipped with a 532 nm laser. The analysis was carried out by doing a 140 μm × 20 μm, *x*, *z* depth scan along the length of the crystal using a 0.57 mm working distance and a 50× objective with a laser spot size of ∼0.5 μm. Raman mapping was done with at a laser setting of 18 mW, an exposure time of 0.5 s, and a step size of 0.5 μm. The resulting spectral image was processed by performing cosmic ray removal and baseline correction. The chemical image was generated from the spectral image by least-squares similarity matching using true component analysis in the WITec software.

Differential Scanning Calorimetry. Approximately 5 mg of samples was heated in a TA Instruments Discovery DSC2500 and heated at 10 °C/min from 25 to 300 °C.

Polarized Light Microscopy. Samples were analyzed using an Olympus BX53B microscopy connected to a computer.

Scanning Electron Microscopy. Samples were deposited onto double-sided silver tape adhered to aluminum scanning electron microscopy (SEM) stubs then coated with ∼10 nm of platinum using a Xenosput coater. Samples were examined with a Hitachi S-4700 scanning electron microscope operating at a 2 kV accelerating voltage.

https://doi.org/10.1021/acs.cgd.1c00399
Cryst. Growth Des. 2021, 21, 4100−4110

RESULTS AND DISCUSSION

Three different sets of studies were carried out to demonstrate mechanistic examples of impurity-induced ripening at different stages in a typical pharmaceutical crystallization. In the first study, the early part of the crystallization was explored, that is, directly after seeding in the presence of five simulated impurities. In this case, only around 45% total amount solids were allowed to crystallize out using an initial supersaturation ratio (concentration/solubility) of 1.8. In the second study, the focus was at the end of the crystallization prior to filtration. The crystallization suspension at 80% yield was allowed to mix under isothermal conditions while tracking changes in purity and particle morphology. The last example of ripening was observable in a so-called post-filtration washing operation in which the filter cake is typically resuspended in an agitated filter dryer. Water was used as the wash solvent, and the impurity levels were similarly monitored over time.

Solubility data of each of the compounds used in this study have been reported earlier,[22] and the simulated impurities were undersaturated at all times in the crystallizations relative to their pure solid phases. The used impurities have been shown in a previous contribution[22] to form solid solutions with SA and hence exhibit a tendency to be retained in the solid phase while also impacting the physical properties of SA.

Example 1: Ripening after Seeding. SA was recrystallized in methanol and water in the presence of five structurally similar compounds simulating typical process impurities. The impurity distribution between the solid and the liquid phases was monitored directly following the onset of crystallization until complete desaturation was achieved. The results from the crystallization are plotted in Figure 1.

All five impurities were entrapped in the solids during the crystallization. The most entrapment was observed of AA, followed by BA, whereas 3HBA and 4HBA and 23DHBA are only present in the solids to a minor extent. Importantly, the impurity entrapment is observed to change significantly during the crystallization in that the entrapment is much higher initially right after seeding and the immediately following secondary nucleation and drop linearly with continued crystallization. These trends are consistent for all impurities. The rate of desupersaturation during the crystallization was fairly rapid and approached the solubility of pure SA after approx. 20 min (inset in Figure 1).

In analyzing the impurity levels at different time points in crystallization, a challenge is to extract the impurity entrapment that occurs at a certain point in time on the surface of the growing crystals. The experimental data that are obtained during the crystallization correspond to a cumulative moving average, that is, from the start of the crystallization to the point of the measurement. This average impurity level, $\bar{\omega}_i^s$, that is experimentally measured and presented in Figure 1, can be written as

$$\bar{\omega}_i^s = \frac{m_i^s}{m_p^S + \sum_{i=1}^{n} m_i^S} \tag{1}$$

where m_is are the masses of impurity i in the solid divided by the mass of product p in the solid plus the mass of all other impurities. However, in order to capture the current impurity entrapment taking place at a certain time in the crystallization, the derivative form is needed. This is henceforth written as ω_is and represents the instantaneous impurity entrapment of impurity i in the solid phase (as $\Delta t \rightarrow 0$)

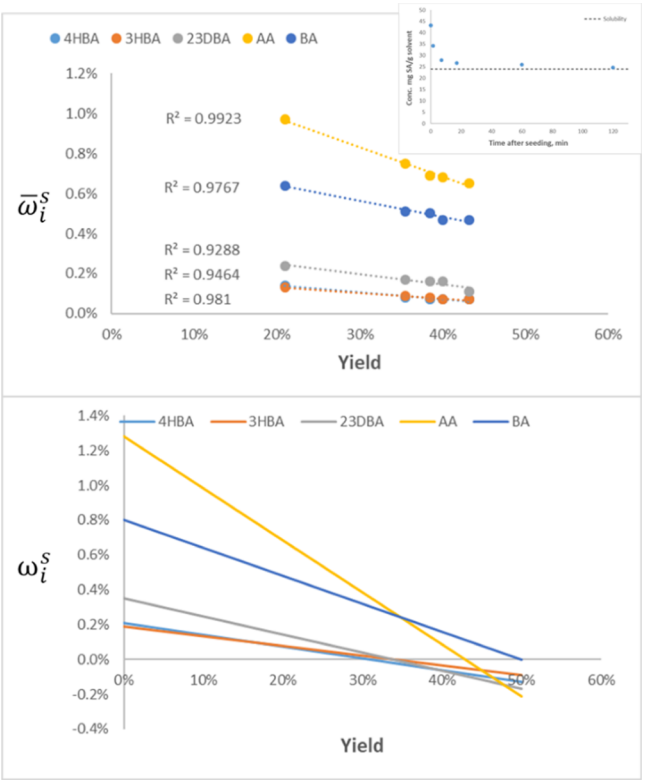

Figure 1. Entrapment of five structurally similar impurities during crystallization of SA following seeding. Top: experimental data with linear regressions. Bottom: derived instantaneous impurity entrapment. Inset: Desupersaturation curve of SA.

$$\omega_i^s = \frac{d(m_i^s)}{d\left(m_p^S + \sum_{i=1}^{n} m_i^S\right)} \tag{2}$$

The distinction provided by eqs 1 and 2 is important as it separates between the impurity entrapment taking place at the surface of the solid phase (or crystals) at a certain time vis-a-vis the bulk. The latter average values can be calculated from the instantaneous impurity entrapment by using the integral form of average from a product yield ranging from 0 to Y_p

$$\bar{\omega}_i^s = \frac{1}{Y_P}\int_0^{Y_P} \omega_i^S \mathrm{d}Y_p \tag{3}$$

Based on the crystallization in Figure 1 showing linear changes in average impurity entrapment with product yield, we can write

$$\bar{\omega}_i^s = qY_P + r \tag{4}$$

where q and r represent the slope and intercept, respectively, and can be determined by regression (regression parameters available in the Supporting Information). If the linearity expressed by eq 4 extends to $Y_p = 0$, then we can solve for ω_is using eqs 3 and 4

$$\omega_i^s = 2qY_P + r \tag{5}$$

Obviously, the difference between the $\bar{\omega}_i$s and ω_is in this example only appears in the doubling of the slope. The change in ω_is can now be plotted versus Y_p for the different impurities, as presented in Figure 1 (bottom). The striking feature with this plot is that the impurity entrapment rapidly approaches and even reaches negative values toward the end of this

https://doi.org/10.1021/acs.cgd.1c00399
Cryst. Growth Des. 2021, 21, 4100−4110

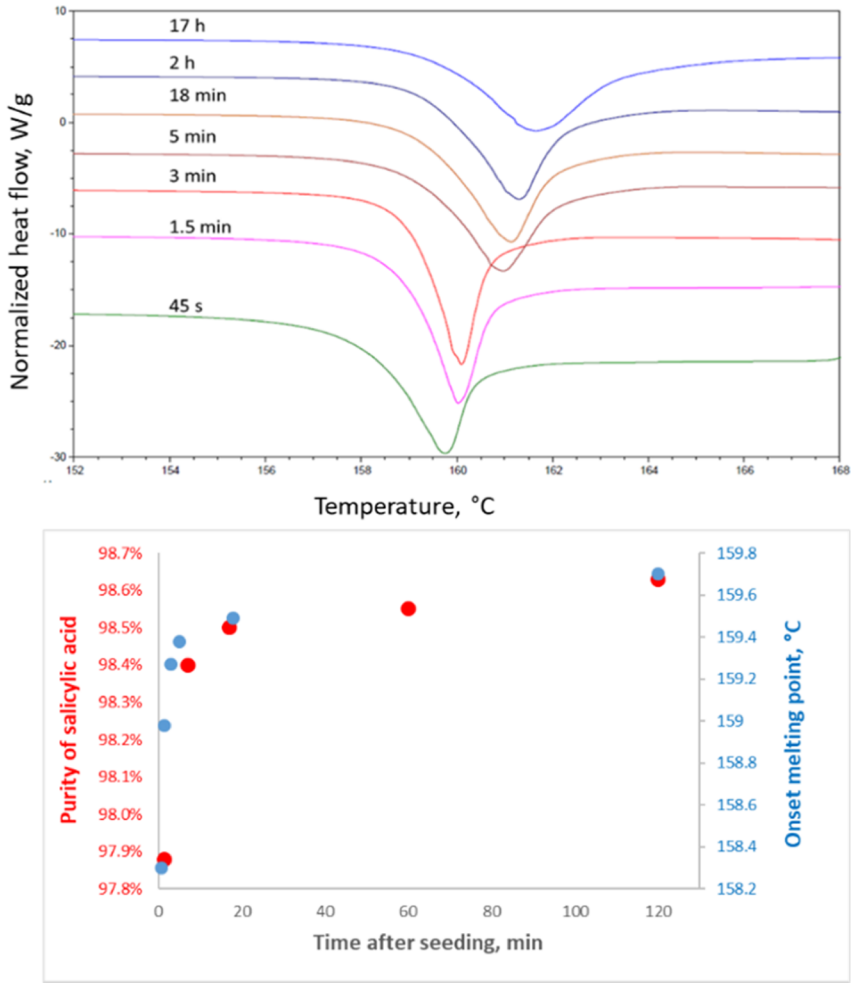

Figure 2. Top: DSC melting endotherms of SA samples pulled at different times after seeding when crystallized in the presence of five structurally similar impurities. Bottom: change in overall purity of SA (red) and onset melting point (blue) during the crystallization.

crystallization. This implies that net amounts of impurities leave the crystals and return to the liquid while solid SA is continuously formed. In other words, the data show that two mass-transfer processes act concomitantly, namely, crystallization of mainly SA and dissolution of solids that are enriched in impurities. While the extent of this varies for different impurities, they all exhibit similar trends and all approach negative impurity entrapment during the crystallization.

The impact on the melting properties of crystallized SA containing entrapped impurities was evaluated in a repeated experiment. Solid samples were collected for differential scanning calorimetry (DSC) analyses focusing on the early part of the crystallization. The results are presented in Figure 2. The onset melting point was at its lowest of 158.30 °C, 45 s after seeding, and increased to its highest value, 159.67 °C, 17 h after seeding. A similar trend occurs for the melting enthalpy, which increased from around 112 J/g up to 143 J/g at the end. In thermodynamic terms, these increases in melting point and melting enthalpy correspond to a lowering of the free energy of the solid phase and hence a reduction in solubility. In addition, the depression in the onset melting points correlates very well with the overall purity of SA (Figure 2 lower graph), which supports the understanding that the ongoing purification of the solid phase is linked to thermodynamic properties.

Microscopy imaging was used to track the morphology of the formed crystals during this crystallization. Thin needles were formed in the early part of the crystallization that increased in thickness and size with continued desupersaturation. After reaching a larger size, cavities began to form in the center at the end of the crystals, which started to propagate in the axial direction toward the core of the crystals, effectively generating hollow crystals (left side in Figure 3). This morphology evolution is reproducible between crystallizations and takes place relatively quickly in this experiment. The hollow crystals are formed at the same time as when the impurities tend to dissolve back in solution. Completely different particle properties were obtained when the same crystallization was repeated without added impurities using SA that has been previously purified by two recrystallizations (right side in Figure 3). In not a single case were hollow crystals observed and all formed crystals were solid throughout exhibiting sharp and distinctive edges. The difference between these two experiments clearly elucidates the role of impurities on the origin of tubular crystal formation.

Example 2: Ripening at the End of Crystallization. In the second example, more than 80% yield was allowed to form through anti-solvent crystallization in MeOH/H_2O, thus representing a typical end condition in a pharmaceutical crystallization process. Only BA was added this time as a simulated impurity, which was done to enable measuring the impurity content in individual crystals using confocal Raman spectroscopy (discussed below). The initial impurity level was

https://doi.org/10.1021/acs.cgd.1c00399
Cryst. Growth Des. 2021, 21, 4100−4110

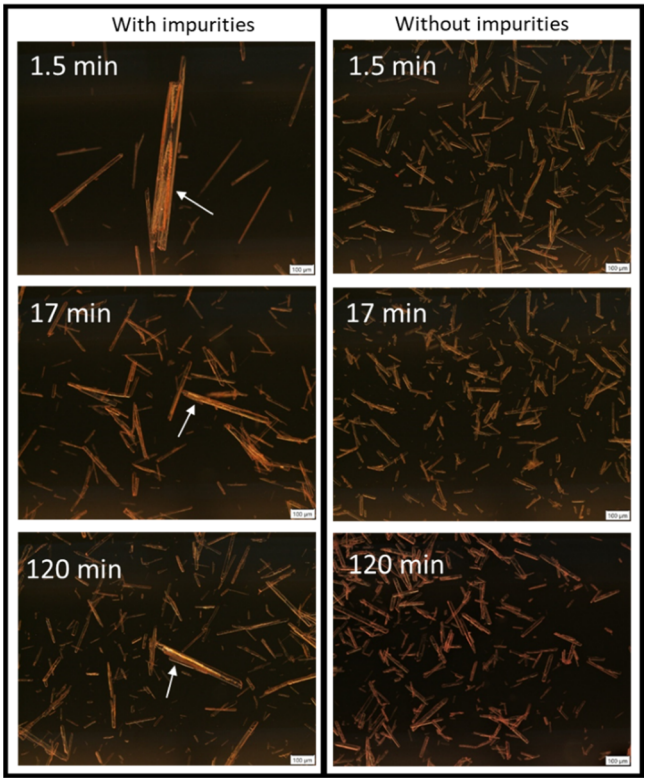

Figure 3. PLM imaging at a 100× magnification of SA crystallized with impurities (left) and without added impurities (right). The time points indicate time after seeding. The crystals were stained with a color agent to better highlight cavities.

5%, which can be compared to a total of 10% impurities in example 1. The suspension formed after seeding was not allowed to equilibrate, and water was added directly until the final solvent composition of 30 wt % MeOH in H_2O was obtained. At this point, samples were collected of the solid and liquid over 5 days.

As shown in Figure 4, the average impurity level in the solid phase began at 1.80% and then over 5 days decreased to around 1.58%. These changes took place even though the

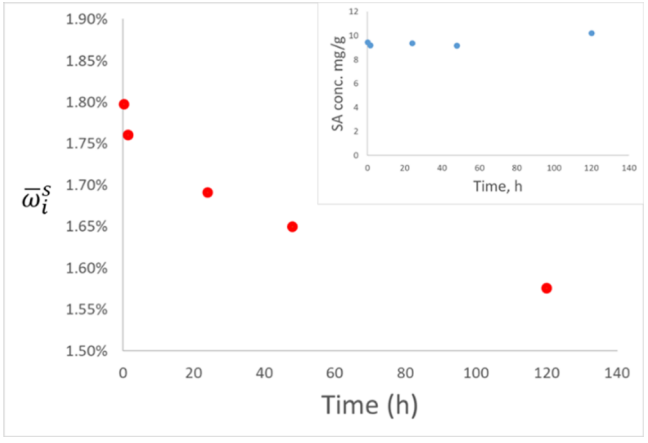

Figure 4. Change in average impurity level in the solid phase over time after reaching 80% yield. The first two samples were pulled 15 and 90 min after reaching the end condition in the crystallization. The inset graph shows the concentration of SA in the liquid phase over time.

solution concentration of SA was constant and seemingly at equilibrium. Just as in the first example, the impurity appears to slowly dissolve back in solution, de facto resulting in purification at constant SA concentration. Compared to example 1, the rate of change is much slower and proceeds over several days.

The same morphological changes were observed in this experiment as in the previous example. Hollow crystals were visible fairly early on and continued to be observed throughout the remainder of the crystallization (left side in Figure 5). A

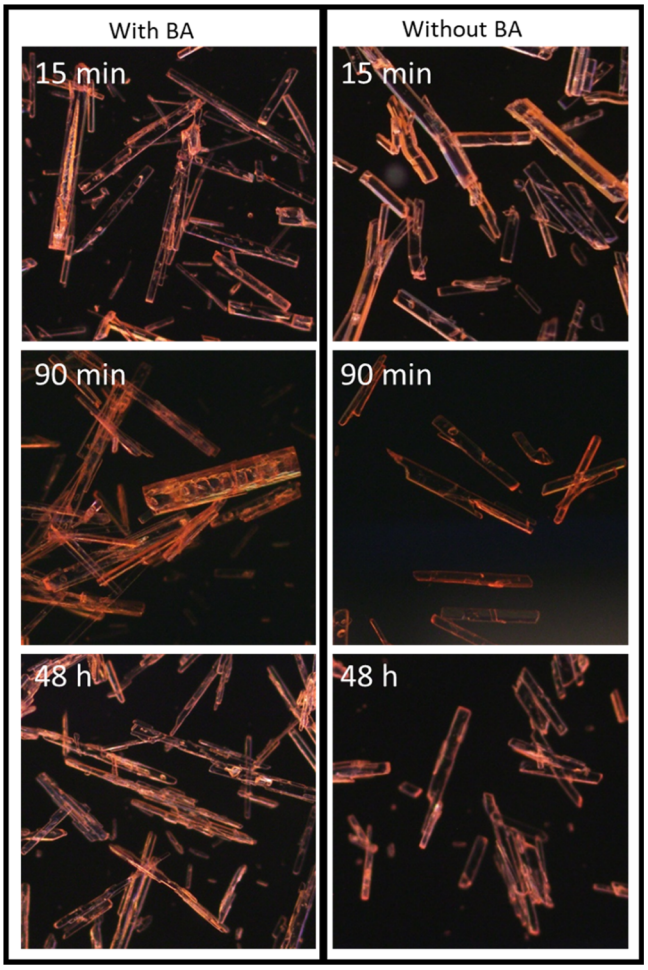

Figure 5. PLM imaging at a 100× magnification of SA crystallized with BA (left) and without BA (right). The time points indicate time after reaching the end condition in crystallization. The crystals were stained with a color agent to better highlight cavities.

close-up of the cavities formed in the center of the crystals is shown by SEM in Figure 6. Repeating this crystallization without impurities did not cause any tubular crystals at all but the same type of transparent well-defined crystals as in example 1 (right side in Figure 5).

It was recently reported[22] that larger inhomogeneities in impurity level of SA were obtained due to changes in the extent of impurity entrapment during the crystallization, as also observed in example 1 above. These variations in purity can be determined using an experimental method referred to as the SLIP test, which is a straightforward experimental test that is based on suspending a solid sample at increasing dilution and measuring the impurity levels in the solid and liquid phases as

https://doi.org/10.1021/acs.cgd.1c00399
Cryst. Growth Des. 2021, 21, 4100−4110

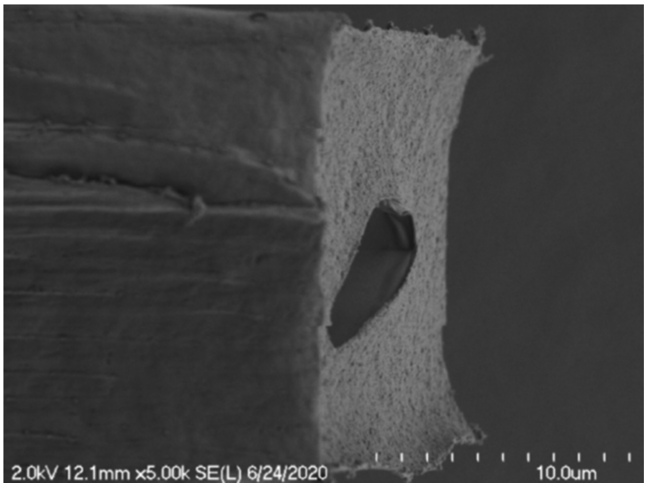

Figure 6. SEM image of the sample pulled after 90 min of SA crystallized with BA (from example 2), highlighting the edge of a crystal. The cavity shown by the darker color in the center of the crystal face corresponds to the entrance to the hollow tunnel.

well as the concentration in the liquid.[23] The obtained material impurity distribution (MID)[22] provides the impurity inhomogeneity of the crystals. Samples pulled after 15, 90 min, and 48 h (in Figure 4) were thus subjected to this test, and the corresponding MIDs were determined. The results are presented in Figure 7.

The resolved MIDs show that BA is highly unevenly entrapped across the material, which is consistent with the previous study[22] and example 1 crystallization above. For example, in the 15 min sample, the average impurity level is 1.80% but ranges by a factor of ca. 4 across the material. These impurity variations become progressively smaller with the later samples at 90 min and 48 h. The impurity inhomogeneity is primarily caused by a smaller subset of the sample (left in main Figure 7), which dissolved first in the SLIP test. The remaining solids exhibit a more uniform impurity distribution closer to the average (right side in main Figure 7). This reduction in the impure subsection of the solids over time is responsible for the overall decrease in the average impurity levels. The impurity inhomogeneity is also reflected in the solubility measurements, which in the 15 min sample changed by 12% from the dirtiest section to the purest. As expected and consistent with changes in melting properties described above, the solubility is the highest when the solids are the dirtiest. Combining these results with the tubular morphology shown in Figures 5 and 6 suggests that most of the impurity domains reside within the core of the crystals, which are released during the ripening leading to the formation of the hollow crystals.

To further corroborate this assertion, Raman spectroscopy was used to analyze the BA level of bulk samples and within individual crystals. Pure BA exhibits a characteristic peak at close to 1000 cm^{-1}, which is distinguishable from SA. The presence of BA integrated in SA crystals is detectable within this frequency range even at lower levels close to the limit of detection (Figure 8).

Confocal Raman imaging allows for gathering spectra down to 0.5 × 0.5 μm sized areas on individual crystals in different dimensions ($x-y$ or $x-z$). Changes in low levels of impurities can thus be detected and measured qualitatively at different positions on the crystal, even below the surface. A crystal was identified from a sample having 4.13% BA on average. The surface of the crystal was indented along its main dimension (Figure 9a: point 3 to 2), which turned into a larger cavity before disappearing below the surface (point 2). Raman spectra in the $x-z$ dimensions were recorded along this line at a depth of 20 μm stretching from ca. 20 μm before the tunnel entrance (point 1) to the end of the ridgeline (point 4). The resulting chemical image determined from the spectral images is presented in Figure 9b,c. The red areas correspond to domains in the crystal that are enriched in BA. The darker shadows in Figure 9b correspond to spectra that are indeterminate from SA and BA. The tunnel formed at the

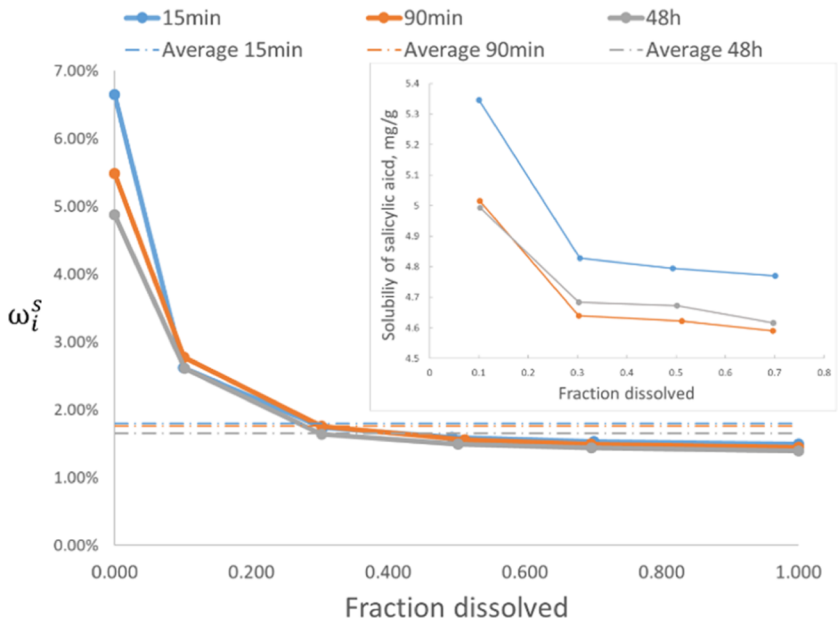

Figure 7. MID of samples from example 2 after 15 min (blue), 90 min (orange), and 2 days (gray) after reaching the end condition in crystallization of SA. The dashed lines correspond to the average impurity level. The measured solubility of SA as a function of dissolved fraction is inserted in the graph.

https://doi.org/10.1021/acs.cgd.1c00399
Cryst. Growth Des. 2021, 21, 4100−4110

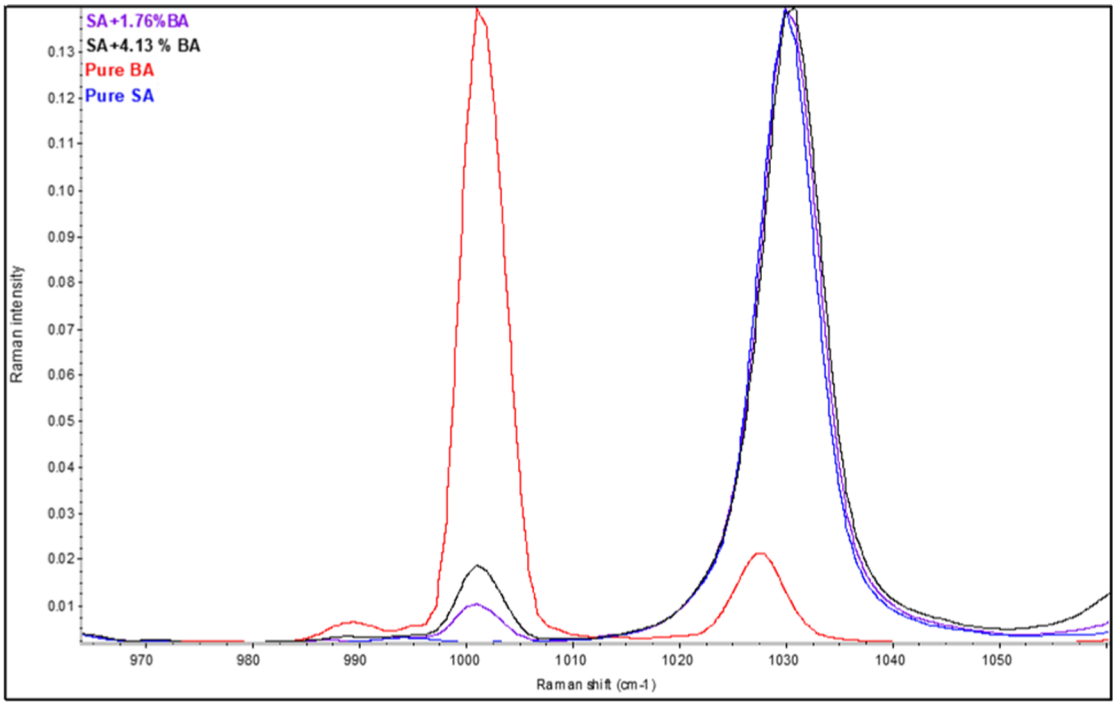

Figure 8. Raman spectra of pure SA (blue), pure BA (red), and SA containing 4.13% BA (black) or 1.76% BA (purple) on average. Recorded with an Agilent TRS 100 with 830 nm laser at a 0.3 s exposure time and 20 accumulations.

surface with a downward trajectory is clearly visible in Figure 9b starting at point 3. Not many enriched BA domains can be seen from point 3 to 2 where the tunnel is exposed and visible from the surface. As the tunnel continues below the surface (point 2 to 1), enriched domains in BA appear all along the trajectory of the tunnel and adjacent to the walls of the tunnel. It appears that the ripening process was largely interrupted before these domains could dissolve back in solution.

Example 3: Ripening during Washing. Agitated filter dryers are widely used in pharmaceutical processing during filtration and washing of the crystallized suspension. Attrition of crystals is common in this unit operation, and hence, in the last example, two types of mechanical mixing environments were evaluated in terms of the impact on releasing the entrapped BA from the core of the crystals. SA was crystallized in the presence of 5% BA per example 2 above, however without allowing the solids to ripen under constant conditions. The isolated solids were instead immediately filtered and dried after the water addition was completed. In the first experiment, SA containing 1.80% BA on average was reslurried in pure water, while being gently stirred using an overhead stirrer at 250 rpm. In the second experiment, SA having 2.15% BA on average was wet-milled in pure water using an IKA T25 wet mill at 4000 rpm, which causes extensive crystal fragmentation. These two experiments represent two extremes in extent of attrition of crystals during agitated filter drying operations. The results are presented in Figure 10.

The difference between the two experiments is striking. BA very slowly leaves the crystals when mixing is mild and crystal attrition is at minimum, as can be seen by the time scale in the left top side of Figure 10. The average impurity levels in the solids started high, in this case at 1.68% after 15 min, and then over around 1 day dropped down until reaching a plateau at 1.61%. Conversely, the concentration of BA increased in the liquid phase over the same time scale. As the concentration of SA was constant (close to 2 mg/g) during the entirety of the experiment, this study constitutes another example of impurity-induced ripening, which demonstrates that this mechanism takes place even during washing of a filter cake without extensive attrition. SEM imaging of the crystals after washing discloses the same typical hollow morphology observed before (Figure 11).

In the second experiment where significant crystal attrition was induced by wet milling, the release of BA was largely completed in only ca. 30 min (right side in Figure 10), which is an order of magnitude faster than that in the first experiment. The average level of BA in the solid phase dropped from 1.90 to 1.82% while the solution concentration exhibited a corresponding increase over time. This rapid purification took place while the solution concentration of SA remained at saturation. These two experiments again show that BA was entrapped within the cores of the crystals but can be quickly released when crystals are broken up exposing the impure inner sections to a dissolving solvent.

Ripening Mechanism. In summary, selective dissolution of impurities associated with changes in particle properties has been observed at all stages of the isolation of SA, namely, the seeding step, the end of the crystallization, and the agitated filter dryer step. This impurity-induced ripening phenomenon is caused by an uneven impurity retention during the crystallization resulting in purity gradients in the solids. In this study, the most impurity entrapment took place directly after seeding. The remainder of the crystallization was associated with significantly less impurity retention. The seeding of pure SA was carried out at a very low level (~0.01%) to more accurately measure the impurity entrapment in the early stages of the crystallization without introducing artifacts from the seeds. Upon seeding, a strong secondary nucleation event inevitably followed giving a thin suspension composed of thin needles. This is arguably the

https://doi.org/10.1021/acs.cgd.1c00399
Cryst. Growth Des. 2021, 21, 4100−4110

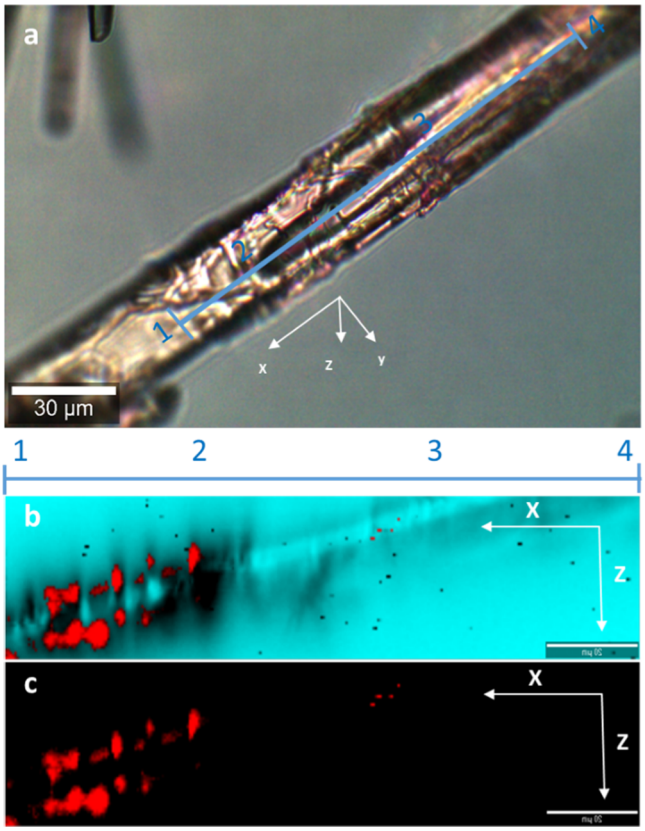

Figure 9. Confocal Raman imaging of an SA crystal with BA incorporated in the crystal. (a): PLM image of the crystal containing the beginning of a tunnel appears to continue below the surface. (b): Chemical image obtained from Raman spectra along the $x-z$ dimension at 140 and 20 μm depths. Red areas correspond to domains enriched in BA within the SA crystal. (c): Chemical image only showing areas with enriched levels of BA.

point where most of the entrapment took place, suggesting a relatively high degree of impurities being involved at the

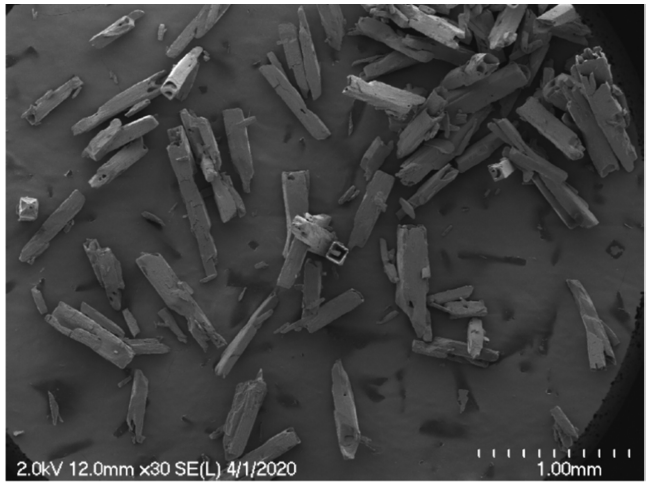

Figure 11. SEM imaging of SA crystallized with BA after 6 days of slurrying in water at ambience (example 3).

nucleation stage. As more of the supersaturation was consumed, crystals became thicker resulting in a reduction in the aspect ratios of the crystals. This crystal growth in the predominately radial direction was associated with less impurity retention and hence the final crystals composed of a dirty core and cleaner outer layers. As the structurally similar compounds used as impurities in this study form solid solutions with SA, the extent of impurity entrapment can be directly linked to its solubility. Each individual crystal that was formed early on carried a solubility gradient wherein the center of the crystals exhibited a higher solubility as compared to the more newly formed outer edges. An intra-particle thermodynamic driving force was thus in effect that under the right conditions could cause selective dissolution of the impure domains of the crystal and recrystallization on the purer areas. These conditions were met in all the examples presented herein. The ripening mechanism can be realized by considering a crystal domain that has formed in the early stages of the crystallization. This segment of the crystal would then contain

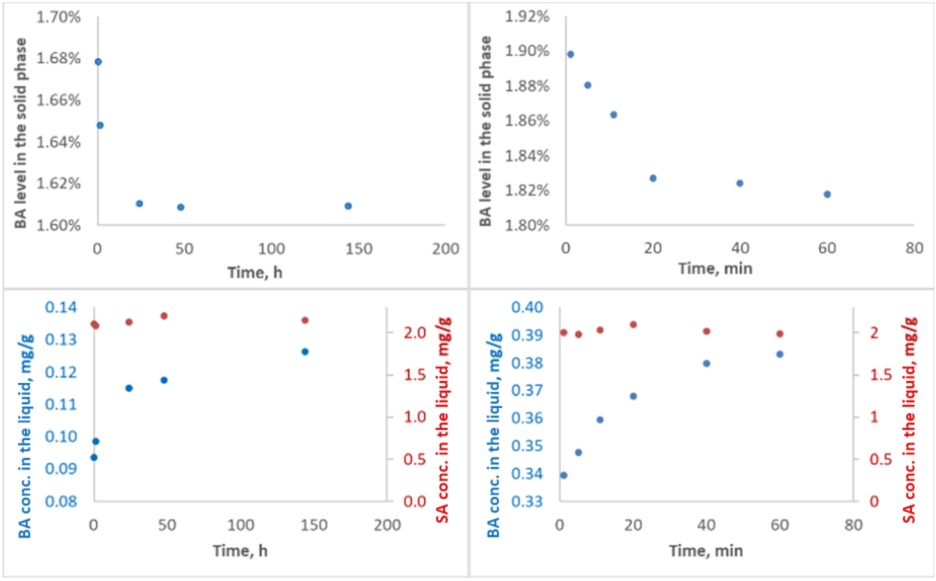

Figure 10. Release of BA under mild overhead mixing (left-side diagrams) vs harsh wet milling (IKA T25, 4000 rpm) (right-side diagrams). Note the difference in time (min vs hours).

https://doi.org/10.1021/acs.cgd.1c00399
Cryst. Growth Des. 2021, 21, 4100−4110

higher levels of impurities and hence higher solubility relative to a pure crystal. As the solution concentration drops toward the solubility of pure SA, the dirtier domains of the crystal now become undersaturated. If this segment of the crystal has access to the surrounding solution, then dissolution will inevitably occur. In fact, when an impurity gradient exists toward the core of the crystal, the initial dissolution will expose domains having even lower purity with higher solubility, which would cause the dissolution to accelerate toward the center of the crystal. Since the solution concentration of SA remained essentially constant in examples 2 and 3, it can be expected that some of the SA that dissolved from the crystal cores recrystallized on the existing crystal surfaces. This recrystallization appears to be associated with significantly less impurity entrapment at similar levels to the entrapment toward the end of the crystallization. These concomitant but opposing mass-transfer processes are thus the origin of the ripening phenomenon responsible for the formation of hollow crystals of SA. An illustration of the impurity-induced ripening mechanism of SA is depicted in Figure 12.

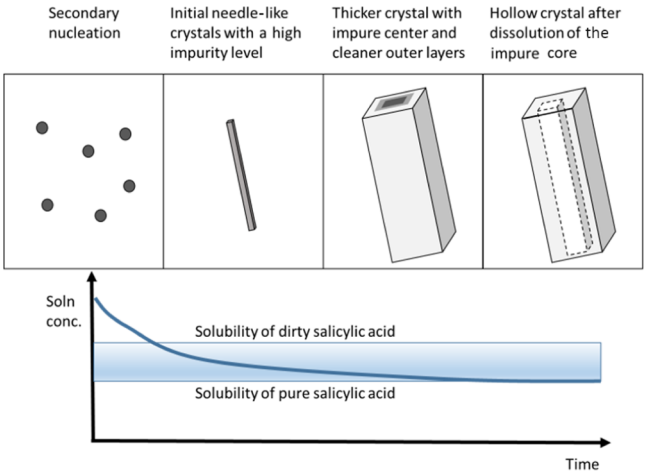

Figure 12. Illustration of the impurity-induced ripening mechanism resulting in the formation of hollow crystals of SA.

For a system like this, the concept of supersaturation cannot be regarded in the traditional way, that is, as a fixed system parameter solely dependent on the solution concentration relative to the solubility at the temperature and solvent composition in question. Each crystal domain exhibits its own intrinsic solubility, which dictates what the actual localized supersaturation ratio will be. This parameter is critical because in the unit operation of crystallization, the supersaturation ratio is the basis for designing, controlling, and understanding the crystallization. An important example of this effect takes place at the seeding step. The seed crystals are typically composed of already crystallized and hence cleaner material. The solubility of the seeds is thus lower than that of the material that crystallizes out initially from the solution, frequently through secondary nucleation. In example 2, the supersaturation ratio at seeding was calculated to be 1.8 based on the solubility of pure SA. The reality, however, is that the solubility of the dirty crystals formed immediately following seeding exhibits a higher solubility. The de facto supersaturation ratio is thus lower. As the crystallization proceeds from that point onward, the solubility of the formed solids decreases at the same time as the solution concentration decreases. This is the dynamic interplay between desupersaturation and solubility that occurs throughout the crystallization of an impure (or real) system. The extent of this effect comes down to the impact of impurity entrapment on solubility of the product. In a previous contribution,[22] the solubility of SA was found to increase by a factor of 2 across the same material when crystallized in the presence of up to seven structurally similar impurities. In example 2 in this report, using only BA as an impurity, the measured solubility increase was 16.5% (inset in Figure 7). Another example has been reported for the inorganic compound $CaCO_3$ with Mg^{2+} as an impurity. In this case, the solubility enhancement was inferred through its impact on step velocity growth.[24] Overall, the understanding of how impurities influence the solubility may not be completely understood and can be difficult to predict. However, whenever impurities are incorporated into the crystal lattice of the product through solid solutions, there is a clear impact on the overall free energy of the crystal lattice, which can be readily observed by its physical properties, for example, crystallinity, melting point, and solubility. These changes reflect how well the impurity molecule can replace the product molecule in the crystal lattice.

As the observed ripening phenomena are linked to the formation of solid solutions with impurities, it is expected that this ripening mechanism may not be exclusive to SA but in fact may be quite general for organic compounds, especially when crystallized in the presence of structurally similar impurities. Another example was recently reported that described variable impurity rejection and dirty crystal cores during the crystallization of the pharmaceutical compound Islatravir.[25] In this case, the dirty crystal cores could be exposed to the surrounding solution and dissolved by breaking the crystals by wet milling and thermal annealing. However, the formation of specifically tubular crystals is directly dependent on the inherent crystal morphology. For SA, the dirty domains of the crystals that were formed initially had access to the surrounding solution after crystal growth due to the needle/bar-like morphology. This allowed for them to dissolve back in solution as the decreasing concentration approached the solubility the pure SA. This situation may not be true of, for example, prismatic crystals, whose dirty cores are less likely to have contact with the solution after continued crystal growth, unless broken up in smaller pieces by, for example, wet milling or other means.

While the impact of impurities on forming hollow crystals is demonstrated in this report, macrotubular crystals have almost exclusively been reported without purposely added impurities or additives.[12−19] The influence of impurities was not the focus of these studies nor monitored. Without repeating these studies and tracking impurities, it should be recognized that no compound is ever completely pure. Impurities are present at all steps in the synthesis and unavoidable in the final product. They are controlled within certain limits based on the assigned specification but never completely absent. A second aspect is that analyses of impurities are routinely measured as average values. As is presented in Figure 7 and was previously reported,[22] the actual impurity distribution within a sample, or even individual crystals, can vary drastically and it is often a smaller subset of the sample that contains much higher levels, depending on how the crystallization was performed. It is also common to have structurally similar impurities in the final product, in part because these are difficult to remove but also because of side reactions and degradations or because the

https://doi.org/10.1021/acs.cgd.1c00399
Cryst. Growth Des. 2021, 21, 4100−4110

unreacted starting material often remains into the final crystallization. Thus, while other reports of forming hollow crystals have not been actively adding impurities, these are undoubtedly still present. In fact, repeating the crystallization in example 1 using SA that was obtained from Sigma-Aldrich without prior purification still resulted in indentations and initial hollowing of crystals, albeit to a much lesser extent, as shown in Figure 13.

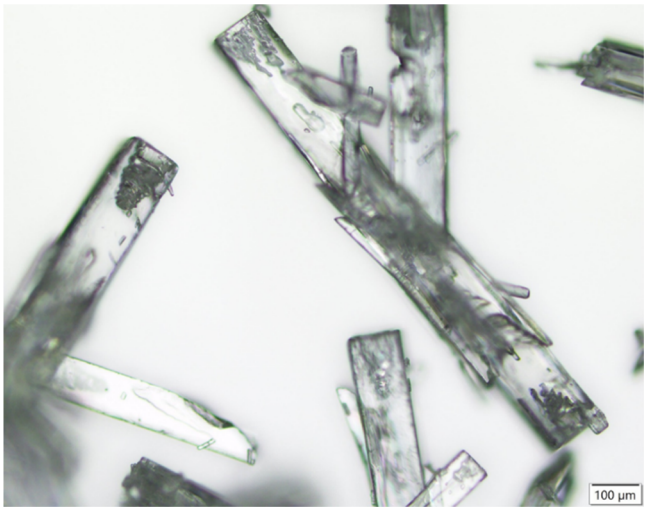

Figure 13. Microscopy image of SA from Sigma-Aldrich recrystallized in MeOH/H_2O as is, without prior purification.

For compounds that do not undergo form conversion, many of the frequently reported underlying factors for causing hollow crystals can be rationalized within the context of impurity-induced ripening. The reason that larger crystals are more likely to contain cavities[13] can be explained by the fact that these crystals would have formed earlier and thus picked up greater gradients in purity during the course of the crystallization as well as had sufficient time to dissolve the dirtier cores. Of course, the detection of cavities is also facilitated with a larger size. Another common parameter expected to influence the formation of hollow crystals is anisotropic crystal growth. As was discussed earlier, the morphology plays a significant role in forming hollow crystals and this is also driven by changes in aspect ratio during the crystallization. Most of the examples in the literature that describe hollow crystals exhibit this morphology.[14,15] A third observation relates to that hollow crystals are often more easily obtained when crystallized at a higher concentration and supersaturation ratio.[13] It is well known that crystallization at higher supersaturation leads to a higher extent of impurity entrapment.[26] As such, larger impurity gradients in the formed crystals are expected that to a higher degree would facilitate the formation of hollow crystals through this ripening mechanism.

CONCLUSIONS

The hollow crystal formation of SA was found to stem from a ripening mechanism that took place due to impurity gradients within individual crystals caused by the formation of solid solutions between the product and structurally similar impurities. This ripening mechanism is different from the Ostwald ripening in terms of the thermodynamic basis and in its applicability across different particle size ranges. The impurity-induced ripening derives from variations in chemical potential within and in between individual crystals, which extends to larger crystals where energetic contributions from surfaces are less pronounced relative to the bulk. The exact lower crystal size limit where this ripening starts to come into play has not been determined. However, based on the crystallizations presented herein, it is clear that most of the variations in impurity entrapment that underpin the ripening phenomenon start with the nucleation event. Whether this is due to involvement of impurities in the nuclei leading up to the onset of nucleation or occurs as a result of elevated impurity entrapment linked to supersaturation has not been established. There is little doubt however, given the thermodynamic nature of the ripening mechanism, that these dissolution and recrystallization effects can be extended to most real crystallizations comprising organic compounds in the presence of structurally similar impurities. As such, crystal morphologies can be engineered, as in the case of hollow crystal formation of SA, and crystallizations can be designed to allow for improved rejection of challenging impurities.

ASSOCIATED CONTENT

Supporting Information

The Supporting Information is available free of charge at https://pubs.acs.org/doi/10.1021/acs.cgd.1c00399.

Regression parameters for equation 4 in example 1, MID calculations from the SLIP test in example 2, additional SEM images from example 2 with and without BA, and additional PLM images from example 3 with and without BA (PDF)

AUTHOR INFORMATION

Corresponding Author

Fredrik L. Nordstrom − *Material & Analytical Sciences, Boehringer-Ingelheim, Ridgefield 06877, Connecticut, United States;* orcid.org/0000-0001-8737-466X; Phone: 1-203-798-4885; Email: fredrik.nordstrom@boehringer-ingelheim.com

Authors

Yongjian Wang − *Chemical and Biomolecular Engineering, University of Connecticut, Storrs 06269-3222, Connecticut, United States*

Huayu Li − *Material & Analytical Sciences, Boehringer-Ingelheim, Ridgefield 06877, Connecticut, United States;* orcid.org/0000-0003-1292-297X

Michelle Raikes − *Material & Analytical Sciences, Boehringer-Ingelheim, Ridgefield 06877, Connecticut, United States*

Brian Linehan − *Material & Analytical Sciences, Boehringer-Ingelheim, Ridgefield 06877, Connecticut, United States*

John Robson − *Material & Analytical Sciences, Boehringer-Ingelheim, Ridgefield 06877, Connecticut, United States*

Complete contact information is available at: https://pubs.acs.org/10.1021/acs.cgd.1c00399

Author Contributions

The manuscript was written through contributions of all authors. All authors have given approval to the final version of the manuscript.

Funding

Boehringer-Ingelheim provided funding for this study.

Notes

The authors declare no competing financial interest.

■ ACKNOWLEDGMENTS

The authors greatly acknowledge the support from Bing-Shiou Yang, Frank Ricci, and David Hirsh.

■ ABBREVIATIONS

SA, salicylic acid; BA, benzoic acid; 23DBA, 2,3-dihydroxybenzoic acid; 3HBA, 3-hydroxybenzoic acid; 4HBA, 4-hydroxybenzoic acid; AA, Anthranilic acid; MeOH, methanol; DSC, differential scanning calorimetry; PLM, polarized light microscopy; SEM, scanning electron microscopy; SLIP, solubility-limited impurity purge; MID, material impurity distribution

■ REFERENCES

(1) Lorenz, R. Lehrbuch der allgemeinen Chemie, von W. OSTWALD. II. Band. 2. Teil: Verwandtschaftslehre. 1. Lieferung. (Leipzig, 1896.) 5 Mark. *Z. Anorg. Chem.* **1897**, *15*, 239.
(2) Ostwald, W. Studien über die Bildung und Umwandlung fester Körper. *Z. Phys. Chem.* **1897**, *22*, 289−330.
(3) Ostwald, W. On the Assumed Isomerism of Red and Yellow Mercury Oxide and the Surface-Tension of Solid Bodies. *Z. Phys. Chem., Stoechiom. Verwandtschaftsl.* **1900**, *34*, 495−503.
(4) Freundlich, H. *Kapillarchemie*; Akademische Verlagsgesellschaft: Leipzig, 1909.
(5) Gibbs, J. W.. The Scientific Papers. Dover: New York, 1961; Vol. *1*.
(6) Volmer, M.; Weber, A. Keimbildung in übersättigten Gebilden. *Z. Phys. Chem.* **1926**, *119*, 277.
(7) Yang, X.; Myerson, A. S. Nanocrystal formation and polymorphism of glycine. *CrystEngComm* **2015**, *17*, 723.
(8) Hou, H.; Xie, Y.; Li, Q. Structure-directing self-organized, one-dimensional ZnO single-crystal whiskers. *Solid State Sci.* **2005**, *7*, 45−51.
(9) Liu, D.; Yates, M. Z. Fabrication of Size-Tunable TiO2 Tubes Using Rod-Shaped Calcite templates. *Langmuir* **2007**, *23*, 10333−10341.
(10) Mallet, F.; Petit, S.; Lafont, S.; Billot, P.; Lemarchand, D.; Coquerel, G. Crystal Growth Mechanism in a Solution of Hollow Whiskers of Molecular Compounds. *Cryst. Growth Des.* **2004**, *4*, 965−969.
(11) Nordström, F. L.; Rasmuson, Å. C. Solubility and melting properties of salicylic acid. *J. Chem. Eng. Data* **2006**, *51*, 1668−1671.
(12) Seidel, J.; Ulrich, J. Generation of Crystalline Microcontainers of Salicylic Acid. *Chem. Eng. Technol.* **2015**, *38*, 984−990.
(13) Tierney, T. B.; Rasmuson, Å. C.; Hudson, S. P. Size and Shape Control of Micron-Sized Salicylic Acid Crystals during Antisolvent Crystallization. *Org. Process Res. Dev.* **2017**, *21*, 1732−1740.
(14) Eddleston, M. D.; Jones, W. Formation of Tubular Crystals of Pharmaceutical Compounds. *Cryst. Growth Des.* **2010**, *10*, 365−370.
(15) Martins, D.; Stelzer, T.; Ulrich, J.; Coquerel, G. Formation of Crystalline Hollow Whiskers as Relics of Organic Dissipative Structures. *Cryst. Growth Des.* **2011**, *11*, 3020−3026.
(16) Pérez-Hernández, N.; Fort, D.; Pérez, C.; Martin, J. D. Water-Induced Molecular Self-Assembly of Hollow Tubular Crystals. *Cryst. Growth Des.* **2011**, *11*, 1054−1061.
(17) Paulino, A. S.; Rauber, G.; Campos, C. E. M.; Maurício, M. H. P.; de Avillez, R. R.; Capobianco, G.; Cardoso, S. G.; Cuffini, S. L. Dissolution enhancement of Deflazacortusing hollow crystals prepared by antisolvent crystallization process. *Eur. J. Pharm. Sci.* **2013**, *49*, 294−301.
(18) Bhargavi, N.; Chavan, R. B.; Shastri, N. R. Hollow crystal generation through polymorphic transformation—a case study of flufenamic acid. *CrystEngComm* **2018**, *20*, 275.
(19) Dette, S. S.; Stelzer, T.; Jones, M. J.; Coquerel, G.; Ulrich, J. Fascinating control of crystalline microstructures. *Chem. Eng. Res. Des.* **2010**, *88*, 1158−1162.
(20) Medina, D. D.; Mastai, Y. Synthesis of DL-Alanine Mesocrystals with a Hollow Morphology. *Cryst. Growth Des.* **2008**, *8*, 3646−3651.
(21) Steele, G. In *Pharmaceutical preformulation and formulation: A practical guide from candidate selection to commercial dosage form*; 2nd edition; Gibson, M., Ed.; Informa Healthcare: New York, NY, USA, 2009; Chapter 6.
(22) Teerakapibal, R.; Li, H.; Linehan, B.; Nordstrom, F. L. Material impurity distribution of lattice-incorporated impurities in salicylic acid. *Cryst. Growth Des.* **2020**, *20*, 1716−1728.
(23) Nordstrom, F. L.; Linehan, B.; Teerakapibal, R.; Li, H. Solubility-limited impurity purge in crystallization. *Cryst. Growth Des.* **2019**, *19*, 1336−1346.
(24) Davis, K. J.; Dove, P. M.; Yoreo, J. J. The role of Mg+2 as an impurity in calcite growth. *Science* **2000**, *290*, 1134.
(25) Sirota, E.; Kwok, T.; Varsolona, R. J.; Whittaker, A.; Andreani, T.; Quirie, S.; Margelefsky, E.; Lamberto, D. J. Crystallization process development for the final step of the biocatalytic synthesis of Islatravir: Comprehensive crystal engineering for a low-dose drug. *Org. Process Res. Dev.* **2021**, *25*, 308−317.
(26) Lorenz, H.; Beckmann, W. Purification by Crystallization. *Crystallization: Basic Concepts and Industrial Applications*; Wiley-VCH Verlag GmbH & Co, 2013; Chapter 7, pp 129−148.

https://doi.org/10.1021/acs.cgd.1c00399
Cryst. Growth Des. 2021, 21, 4100−4110